Applied Nanoscience (2020) 10:1501–1510
https://doi.org/10.1007/s13204-019-01218-8

ORIGINAL ARTICLE

Development of $CuCr_2O_4$ nanocomposite adopting decoration with polyaniline for acridine orange dye degradation

A. Baoum[1] · M. S. Amin[2,3] · R. M. Mohamed[1,4]

Received: 17 October 2019 / Accepted: 5 November 2019 / Published online: 23 November 2019

Abstract

In this investigation, polyaniline@$CuCr_2O_4$ nanocomposites possessing diverse mass proportions of polyaniline (PANI): $CuCr_2O_4$ were fabricated. The photocatalytic action of the diverse synthesized specimens throughout the photocatalytic decadence of acridine orange beneath Vis light illumination was elucidated. Consolidating polyaniline to $CuCr_2O_4$ nanospheres diminishes their specific surface areas from 100 to 90 m^2/g. TEM micrographs acknowledged that both $CuCr_2O_4$ and polyaniline@$CuCr_2O_4$ nanocomposites have arisen as compatible nanospherical. It has been conducted that incorporating PANI to $CuCr_2O_4$ photo-catalyst did not alter the nanocomposites structure of the base $CuCr_2O_4$. Furthermore, the microscopic content loading of PANI onto the surface of $CuCr_2O_4$ makes it hard to be clearly monitored. The photocatalytic disintegration of acridine orange dye underneath Vis light illumination practicing 0.06% polyaniline/$CuCr_2O_4$ nanocomposites has reached 100% after 40 min adopting 2.0 g/L photo-catalyst dosage.

Keywords $CuCr_2O_4$ · PANI · Visible photo-catalyst · Acridine orange dye

Introduction

In the contemporary society, as long as there is population growth and expanding diverse industries there is an enlarged interest regarding environmental deterioration. Accordingly, many reviews have been assigned to expand highly adequate environmental degeneration approaches (Reddy et al. 2016; Rani et al. 2017; Haghighat Mamaghani et al. 2017; Szczepanik 2017). One of the most extensive compounds that engender environmental pollution is acridine orange (AO) dye. Acridine orange is a compound that could be utilized for diverse purposes like dyeing, lithography, leather manufacturing and printing ink (Xie et al. 2000). In addition, acridine orange (AO) dye has diverse biological applications (Girish et al. 2017). Simple methods of wastewater treatment failed to remediate acridine orange (AO) dye. Actually, the existence of this dye in wastewater poses a contemplative issue as it represents a major origin of aquatic pollution (Faisal et al. 2007). And so, assisting efficient design to remove this pollutant from aquatic environment has become an issue of great concern. Discrete regimes have been devoted to remediate this dye from environment including; advanced oxidation, electrochemical treatment, photolysis, chemical precipitation, chemical oxidation, etc. (Peng and Fan 2005). As long as it has great efficacy, advanced oxidation has been developed as one of the most meaningful approaches for dye deportation from wastewater. Obviously, advanced oxidation technique depends primarily on generation of active hydroxyl radicals by the aid of numerous manners like TiO_2-interfered photocatalysis and O_3/H_2O_2/UV, H_2O_2/UV, H_2O_2/Vis photolysis. Photo-catalysis, especially that of heterogeneous kind, has become one of the most relevant techniques to treat wastewater as it could effectively degrade pollutants beneath mild conditions and low-cost expenses generating harmless compounds (Szczepanik 2017; Chen and Cao 2005; Faisal et al. 2019). The heterogeneous photocatalyst should acquire so low bandgap energy (less than 3.0 eV) that it could absorb

✉ R. M. Mohamed
redama123@yahoo.com

[1] Department of Chemistry, Faculty of Science, King Abdulaziz University, PO Box 80203, Jeddah 21589, Saudi Arabia

[2] Chemistry Department, College of Science, Taibah University, Taibah, Saudi Arabia

[3] Chemistry Department, Faculty of Science, Ain Shams University, Cairo, Egypt

[4] Advanced Materials Department, Central Metallurgical R&D Institute, CMRDI, P.O.Box 87, Helwan, Cairo, Egypt

solar energy and hence it would be adopted in diverse applications (Wang et al. 2017). Nevertheless, the well-known photocatalysts (ZnS, ZnO, and TiO_2) that absorb only in UV zone are noticeable as impoverished photo-catalyst beneath Vis light irradiation (Girish et al. 2017; Faisal et al. 2007; Peng and Fan 2005). Therefore, several attempts have been performed to design efficient photocatalysts in the Vis zone (Wang et al. 2017; An et al. 2016; Meng and Zhang 2016; Sohabi et al. 2017; Aljahdali et al. 2018; Sobahi et al. 2018; Baoum et al. 2018; Sobahi and Amin 2019a, b). Among the recently designed photocatalysts for various purposes like super-capacitors, photocatalytic destruction of dyes, thermal decomposition reactions, and photocatalytic hydrogen evolution is copper chromite ($CuCr_2O_4$) photo-catalyst that acquires narrow bandgap energy (Yan et al. 2009; Yuan et al. 2014; Acharyya et al. 2015a, b, c; Paul et al. 2015; Sanoop et al. 2015; Mageshwari et al. 2015; Ma et al. 2016). Numerous successful approaches have been investigated to fabricate $CuCr_2O_4$ like; sol–gel (Lee et al. 2016), solid-state (Arboleda et al. 2014), co-precipitation (Delmon 2007) and hydrothermal (George and Sugunan 2008) regimes. Some features restrain the capability $CuCr_2O_4$ to be adopted in various applications like its limited light absorption. Thus, the challenge is the development of an efficient strategy to boost the photocatalytic activity of $CuCr_2O_4$ by modifying its efficiency to absorb light. Polyaniline (PANI) has been devoted to the photocatalytic operations as a result of its amazing aspects like its great capability to absorb Vis light, the exclusive transporting characteristics of its electrons and holes, its low price and the ease methods of its synthesis in comparison to decorating rare metals. Diverse reviews concluded that inclusion of PANI to photo-catalyst could boost the migration efficacy of charge transporters amid photocatalyst and PANI. Many attempts have been achieved for constructing efficient nanocomposite decorated with polyaniline for example; PANI/$BiVO_4$ (Shang et al. 2009), PANI/TiO_2 (Radoicic et al. 2017), PANI/ZnO (Zhang et al. 2009), PANI/BiOCl (Wang et al. 2013), Ag_3PO_4@PANI (Liu et al. 2017) and PANI@CdS (Zhang and Zhu 2010). And so, $CuCr_2O_4$ could be modified via doping with PANI and the modification may involve extension of its light absorption zone as well as enhancement of the separation of the charge carriers which certainly leads to improved photocatalytic action. In this investigation, PANI/$CuCr_2O_4$ nanocomposite of excellent capability towards Vis light absorption has been established. The photocatalytic activity of the fabricated nanocomposite has been assessed via destruction of acridine orange dye beneath Vis light. The interface interaction amid $CuCr_2O_4$ and PANI might be the reason for the boosted photocatalytic destruction performance over PANI/$CuCr_2O_4$ nanocomposite. In addition, long-wavelength of illuminated light has been adopted to assure that inclusion of PANI broadens the light absorption zone with great efficacy.

Materials and experimental designs

Materials

All adopted chemicals in this examination were of analytical grade and were utilized as received. Aniline, absolute ethanol, ammonium persulphate and citric acid of about 99.5% purity were utilized. In addition, highly pure (96%) sodium hydroxide was applied. Besides, two different nitrate salts (copper nitrate tri-hydrate and chromium nitrate nonahydrate) and tetrahydrofuran (THF) were handled.

Photocatalysts Fabrication

Fabrication of PANI

The polymerization process at mild temperature has been addressed to attain PANI. Deionized water (80 mL) was utilized to dissolute definite quantity of citric acid and the resultant mix was agitated for about 20 min. After that, aniline (0.5 mL) was introduced to the previously prepared solution and the resultant mixture was agitated for about 0.5 h. Then, 20 mL of ammonium persulfate solution (0.25 M) was incorporated dropwise to the produced mix and the attained solution was agitated for 24 h. The temperature all over the investigation was kept between 0–5 °C. After all, the specimen was gathered, washed with ethanol many intervals and then left to dry for 6 h at 60 °C. Polyaniline (PANI) powder of green color has been received.

Fabrication of $CuCr_2O_4$ nanospherical

Deionized water (50 mL) was utilized to dissolute chromium nitrate nonahydrate (15.4 g) and copper nitrate tri-hydrate (5.54 g) to receive 1 M solution of the analogous nitrates. The resultant solution was intermixed with deionized water together with 1 M sodium hydroxide solution (50 mL) at 60 °C. pH was adjusted to be 7 amid precipitation. After reaction completion, the precipitate was left in the mother liquor for 5 h. After that, the produced system was dried at 90 °C and the yield was fired for 5 h at 500 °C to receive $CuCr_2O_4$ nanospherical.

Fabrication of $CuCr_2O_4$ nanocomposite decorated with PANI

$CuCr_2O_4$ photocatalysts decorated with PANI were designed at ambient temperature. $CuCr_2O_4$ powder (2.0 g) was introduced to 0.22 g L^{-1} PANI/THF solution (0.75 mL) and the resultant mix was dissolved in ethyl alcohol (30 mL). After that, 2 M sodium hydroxide (15 mL) was incorporated dropwise to the former solution under constant agitation

that extended for 4 h. The attained solution was washed at numerous intervals with deionized water and left to dry for 24 h at 60 °C. Evidently, the gathered specimen of PANI/$CuCr_2O_4$ was designated as 0.02% PANI/$CuCr_2O_4$ nanocomposite (mass proportion of PANI: $CuCr_2O_4$ = 0.02%). In a similar way, different PANI/$CuCr_2O_4$ nanocomposites acquiring diverse mass proportions of PANI:$CuCr_2O_4$ as 0.04%, 0.06% and 0.0.08% were fabricated and designated as 0.04% PANI/$CuCr_2O_4$, 0.06% PANI/$CuCr_2O_4$ and 0.08% PANI/$CuCr_2O_4$ nanocomposites, respectively.

Characterization

XRD appliance was applied to interpret the crystalline phases of the fabricated specimens. Whereas, FTIR spectrometer was appropriated to register the transmittance mode of the FTIR spectra at room temperature. For X-ray photoelectron spectroscopy (XPS) assessments, a Thermo Scientific spectrometer was supported. In addition, transmission electron microscopy (TEM) of JEOL kind was devoted to analyzing the morphology as well as the architecture of the diverse fabricated specimens. Chromatech appliance of Nova 2000 kind was practiced to interpret the textural aspects of the formulated specimens. Moreover, bandgap magnitudes were assessed (estimated from diffuse reflectance spectra) via covering UV–Vis–NIR spectrophotometer. The fluorescence spectrophotometer (Shimadzu model) was supported to record the photoluminescence emission spectra (PL). Finally, Zahner Zennium electrochemical workstation was affirmed to register the transient photocurrent measurements.

Photocatalytic Examination

In this examination, an acridine orange (AO) dye was chosen as a typical example of pollutant to test its photocatalytic destruction over $CuCr_2O_4$ nanocomposite decorated with polyaniline. A concentration of 100 ppm corresponding to the degraded dye has been chosen and a Xe-arc lamp, that emits UV–Vis radiation, was selected to be the light source. In the photocatalytic investigation, we allow only the Vis light to be absorbed by the tested photocatalyst and so, UV light was prevented from absorption via utilization UV cut filter. 0.5 L of the tested dye (100 ppm) was blended with nanocomposite ($CuCr_2O_4$ decorated with polyaniline) and the system was continuously pumped by air to assure the existence of oxygen all over the reaction. The mix was continuously agitated for 0.5 h in dark to attain equilibrium of adsorption/desorption of the tested dye solution prior to irradiation. After that, the previous system was subjected to irradiation via the mentioned light source for 1 h. after definite intervals, 3 mL of suspension was extracted from the reaction medium. Centrifugation was performed to the withdrawn solution to detach the solid. Hence, UV/Vis/NIR spectrophotometer was utilized to record the absorbance of the diverse specimens at 492 nm.

Results and discussion

XRD spectra were implemented to diagnose the crystallinity and phase composition of the fabricated neat $CuCr_2O_4$ as well as PANI@$CuCr_2O_4$ nanocomposite specimens (Fig. 1). XRD patterns of Fig. 1 reveal the presence of (112) (211) (202) (224) and (303) crystal planes correspond to neat $CuCr_2O_4$ (JCPDS 05-0657). On the other hand, no prescribed peaks of PANI were registered in the diffractograms of Fig. 1. This observation could be attributed to the very limited amount of the applied PANI in the nanocomposite. Furthermore, alteration of the intensities correlated to some diffractograms as a result of boosting the PANI dose has been observed. This alteration in intensity might be associated with the particle size reduction of $CuCr_2O_4$ nanospherical as the result of enlargement of its degree of dispersion (Zhang et al. 2009).

The occupation $CuCr_2O_4$ by PANI in the PANI@$CuCr_2O_4$ nanocomposite might be confirmed through establishing FTIR analyses. Figure 2 exhibits FTIR spectra data of PANI, neat $CuCr_2O_4$ as well as PANI@$CuCr_2O_4$ specimens. It is clear that the FTIR spectrum of neat $CuCr_2O_4$ exhibits a strong absorption peak at 522 cm^{-1}, this peak is associated with the stretching mode of the Cu–O bond (Zhao et al. 2017). Whereas, FTIR spectrum of PANI displays numerous absorption peaks located at 1584, 1496, 1415, 1300 cm^{-1}, 1104 and 617 cm^{-1}. Evidently, existence of quinoid and benzenoid stretching rings could be verified via the appearance of the peaks located at 1584, 1496 and 1415 cm^{-1}. Whereas, stretching vibration mode of C–N corresponding to benzenoid unit might be documented through

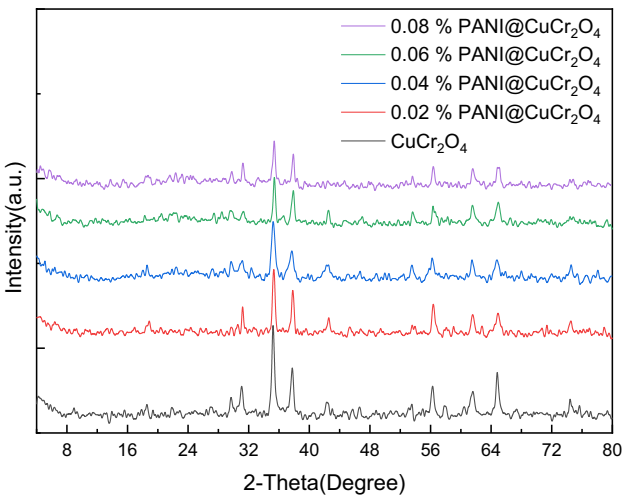

Fig. 1 XRD patterns of $CuCr_2O_4$ and PANI@$CuCr_2O_4$ samples

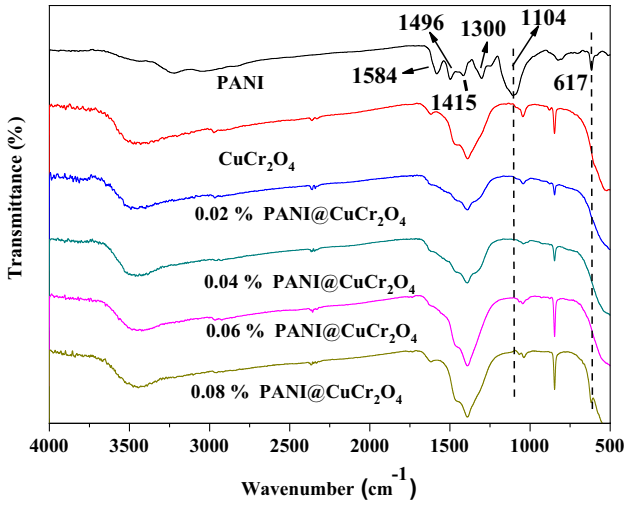

Fig. 2 FT-IR spectra of pure $CuCr_2O_4$, PANI and PANI@$CuCr_2O_4$ samples

the emerging of the band located at 1300 cm^{-1}. Furthermore, the bands found at 1104 cm^{-1} and 617 cm^{-1} could be associated with C–H bending vibration mode (Zhang et al. 2009; Tanwar et al. 2017). On the other hand, FTIR spectrum of PANI@$CuCr_2O_4$ nanocomposite displays two distinct bands at 1104 and 617 cm^{-1} in addition to extra peaks similar to those of pure $CuCr_2O_4$ photocatalyst. The appearance of distinct absorption peak at 1104 cm^{-1} is associated with the stretching vibration mode of CAN in the benzenoid unit in PANI, whereas, the absorption peak located at 617 cm^{-1} could be correlated to the bending vibration mode of CAH. These findings confirm strongly the habitation of PANI in the fabricated PANI@$CuCr_2O_4$ nanocomposite. Obviously, the occurrence of extra peaks in FTIR spectrum of PANI@$CuCr_2O_4$ similar to those of pure $CuCr_2O_4$ affirms the inclusion of PANI to $CuCr_2O_4$ to fabricate PANI@$CuCr_2O_4$ does not alter the skeleton of $CuCr_2O_4$.

XPS spectra of 0.06% PANI@$CuCr_2O_4$ nanocomposite are displayed in Fig. 3. Figure 3a confirms that PANI@$CuCr_2O_4$ nanocomposite specimen enclose Cu, Cr, O, C and N elements within its structure. Whereas, Fig. 3b displays two characteristic spectral peaks located at 935.2 and 954.0 eV and might be correlated to the Cu2p high-resolution. In fact, Cu2p3/2 and Cu2p1/2 could be verified via the appearance of these peaks (at 935.2 and 954.0 eV, respectively). This finding reflects the oxidation state of Cu^{2+} in 0.06% PANI@$CuCr_2O_4$ nanocomposite. On the other hand, Fig. 3 C displays two distinct spectral peaks located at 574.5 and 583.9 eV that could be associated with Cr2p3/2 and Cr2p1/2, respectively. This observation confirms the oxidation state of Cr^{3+} in 0.06% PANI@$CuCr_2O_4$ nanocomposite. Furthermore, the confirmation of O 1 s existence could be achieved via the peak located at 532.5 eV that reflects the oxidation state of O^{2-} in 0.06% PANI@$CuCr_2O_4$ nanocomposite (Fig. 3d). Finally, the presence of polyaniline in the fabricated nanocomposite could be confirmed via the appearance of the peaks located at 400 and 284.7 eV for N 1 s and C 1 s (Fig. 3e, f, respectively).

Figure 4 exhibits TEM images of pure $CuCr_2O_4$ as well as PANI@$CuCr_2O_4$ specimens. It is elucidated from the data of Fig. 4 that the dominated shape in all illustrated morphologies is the nanospherical morphology. Furthermore, it is noticed that the inclusion of PANI to $CuCr_2O_4$ has a negative effect on $CuCr_2O_4$ particle size (Fig. 4b–e). on the other hand, it is noticed that inclusion of different doses of PANI to $CuCr_2O_4$, to fabricate various PANI@$CuCr_2O_4$ specimens, has no obvious consequence on the morphological structures of the diverse PANI@$CuCr_2O_4$ nanocomposites. The tiny dose of PANI explains the absence of the morphology corresponding to PANI in the TEM images of the fabricated PANI@$CuCr_2O_4$ nanocomposites.

Figure 5 exhibits HRTEM images for 0.06% PANI@$CuCr_2O_4$ specimen. It is concluded from the presence of lattice spacing at 0.476 nm, which characterizes the plane of (101) of $CuCr_2O_4$, that the major phases in PANI@$CuCr_2O_4$ specimen are $CuCr_2O_4$. On the other hand, the very low dose of PANI included in the PANI@$CuCr_2O_4$ specimen explains the absence of the lattice spacing corresponding to PANI.

Table 1 depicts the BET values for pure $CuCr_2O_4$ as well as the diverse PANI@$CuCr_2O_4$ nanocomposites. It is clear from the data tabulated in Table 1 that the specific surface areas of pure $CuCr_2O_4$, 0.02% PANI@$CuCr_2O_4$, 0.04% PANI@$CuCr_2O_4$, 0.06% PANI@$CuCr_2O_4$ and 0.08% PANI@$CuCr_2O_4$ specimens are in the sequence of 100.00, 98.00, 95.00, 93.00 and 90.00 m^2/g. The lower specific surface areas of the specimens accommodating PANI compared to that of the pure $CuCr_2O_4$ clarifies that inclusion of PANI to $CuCr_2O_4$ has a negative effect on the specific surface areas corresponding to $CuCr_2O_4$.

Figure 6 shows the UV–Vis spectra of the pure $CuCr_2O_4$ and PANI@$CuCr_2O_4$ specimens. It is obvious from the data of Fig. 6 that the absorption zones for the pure $CuCr_2O_4$, 0.02% PANI@$CuCr_2O_4$, 0.04% PANI@$CuCr_2O_4$, 0.06% PANI@$CuCr_2O_4$ and 0.08% PANI@$CuCr_2O_4$ specimens are corresponding to visible light. Evidently, the bandgap magnitudes of the diverse fabricated specimens could be resolved from their UV–Vis spectral curves (Table 2). The bandgap magnitudes are found to be 2.12, 2.00, 1.92, 1.73 and 1.72 eV corresponding to the pure $CuCr_2O_4$, 0.02% PANI@$CuCr_2O_4$, 0.04% PANI@$CuCr_2O_4$, 0.06% PANI@$CuCr_2O_4$ and 0.08% PANI@$CuCr_2O_4$ specimens, respectively. Hence, it could be concluded that band gap magnitude of the $CuCr_2O_4$ specimen is declined when PANI is included in the $CuCr_2O_4$ to form PANI@$CuCr_2O_4$ specimens. In general, decline of bandgap energy brings about

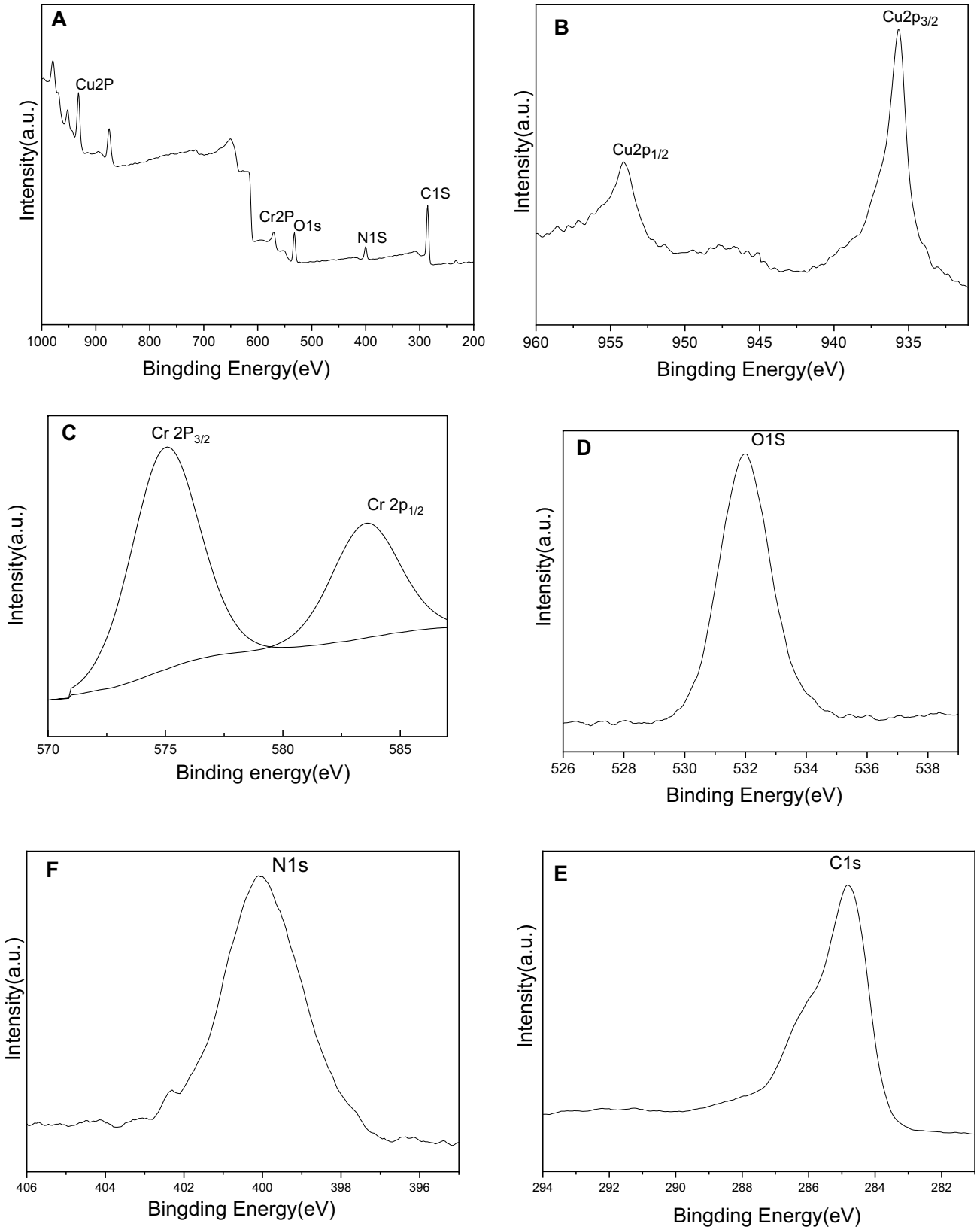

Fig. 3 XPS spectra for survey scan spectra (**a**), high-resolution spectra of Cu2P (**b**), Cr2p (**c**), O1S (**d**), NIS (**e**) and C1S (**f**) of 0.06% PANI@ $CuCr_2O_4$ sample

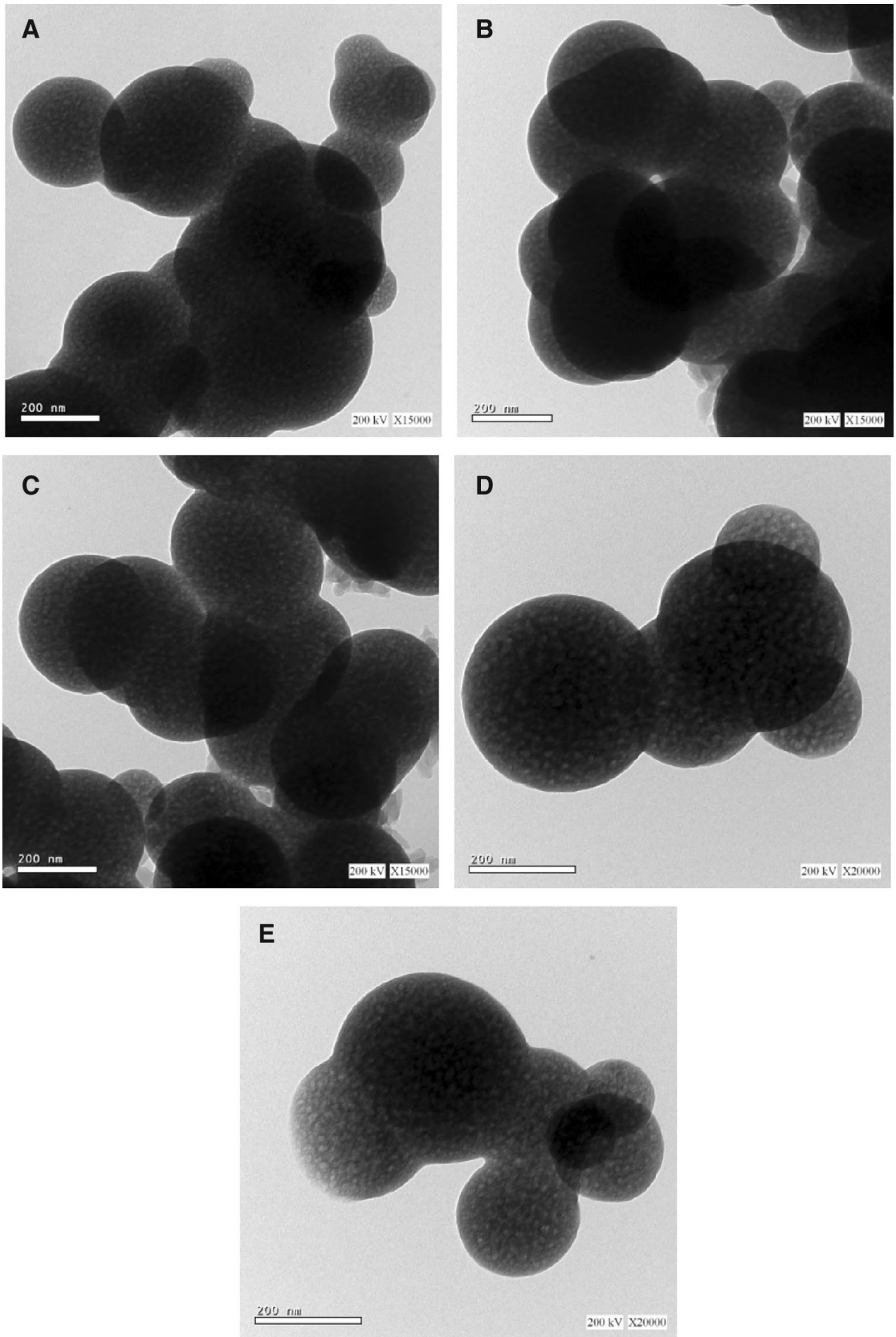

Fig. 4 TEM images of $CuCr_2O_4$ (**a**) 0.02% PANI@$CuCr_2O_4$ (**b**) 0.04% PANI@ $CuCr_2O_4$ (**c**) 0.06% PANI@$CuCr_2O_4$ (**d**) and 0.08% PANI@ $CuCr_2O_4$ (**e**) samples

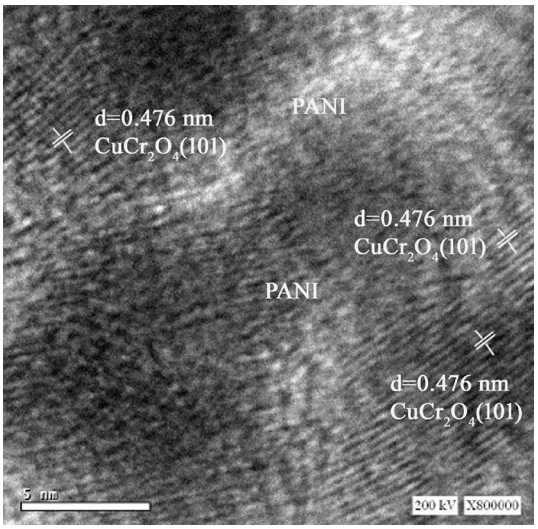

Fig. 5 HRTEM image of 0.06% PANI@$CuCr_2O_4$ sample

Table 1 BET surface areas of $CuCr_2O_4$ and PANI@$CuCr_2O_4$ samples

Samples	BET surface area, m^2/g
$CuCr_2O_4$	100.00
0.02% PANI@ $CuCr_2O_4$	98.00
0.04% PANI@ $CuCr_2O_4$	95.00
0.06% PANI@ $CuCr_2O_4$	93.00
0.08% PANI@ $CuCr_2O_4$	90.00

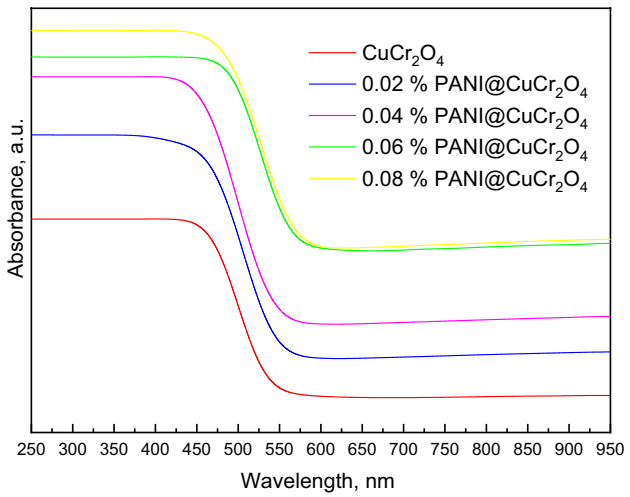

Fig. 6 UV–Vis spectra of the $CuCr_2O_4$ and PANI@$CuCr_2O_4$ samples

an enhancement in the photocatalytic reactivity of the fabricated PANI@$CuCr_2O_4$ nanocomposites.

Table 2 Band gap energies of $CuCr_2O_4$ and PANI@$CuCr_2O_4$ samples

Sample	Bandgap, eV
$CuCr_2O_4$	2.12
0.02% PANI@$CuCr_2O_4$	2.00
0.04% PANI@$CuCr_2O_4$	1.92
0.06% PANI@$CuCr_2O_4$	1.73
0.08% PANI@$CuCr_2O_4$	1.72

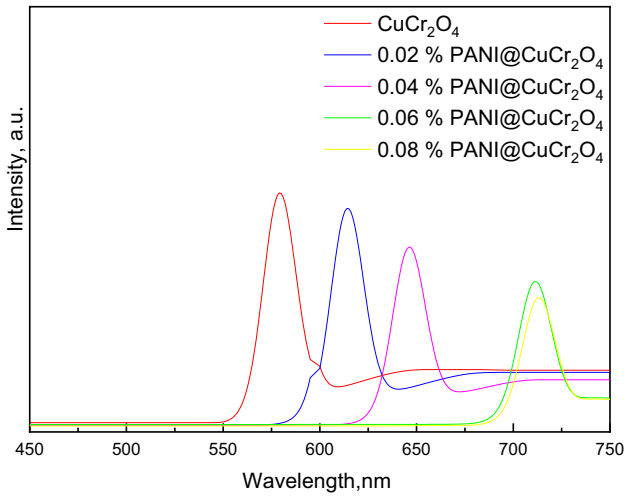

Fig. 7 PL spectra of the $CuCr_2O_4$ and PANI@$CuCr_2O_4$ samples

The PL spectra of pure $CuCr_2O_4$, as well as PANI@CuCr2O4 specimens, are interpreted in Fig. 7. The outcomes of Fig. 7 clarify that the $CuCr_2O_4$ specimen possesses high emission peak intensity announcing that the reconsolidation speed of the photo-generated charge transporters of the pure $CuCr_2O_4$ specimen is high. Whereas, the intensities of emission peaks for the diverse PANI@$CuCr_2O_4$ nanocomposites are small when correlated to that of the pure $CuCr_2O_4$ specimen. It is noticed that the intensities of the different peaks are in the order of; $CuCr_2O_4$ > 0.02% PANI@$CuCr_2O_4$ > 0.04% PANI@$CuCr_2O_4$ > 0.06% PANI@$CuCr_2O_4$ > 0.08% PANI@$CuCr_2O_4$. Accordingly, 0.06% PANI@$CuCr_2O_4$ specimen possesses the lowest emission peak intensity compared to those of other specimens. Besides, the reconsolidation speed of the photo-generated transporters is very small for the same specimen (0.06% PANI@$CuCr_2O_4$ sample) that brings about an enhancement of its photocatalytic efficacy.

Transient photocurrent responses of the fabricated $CuCr_2O_4$ and PANI@$CuCr_2O_4$ specimens are displayed in Fig. 8. The attained responses reflect that $CuCr_2O_4$ specimen possesses low photocurrent intensity. This finding suggests that the recombination speed of the photo-generated charge carriers for the $CuCr_2O_4$ specimen is high. On the

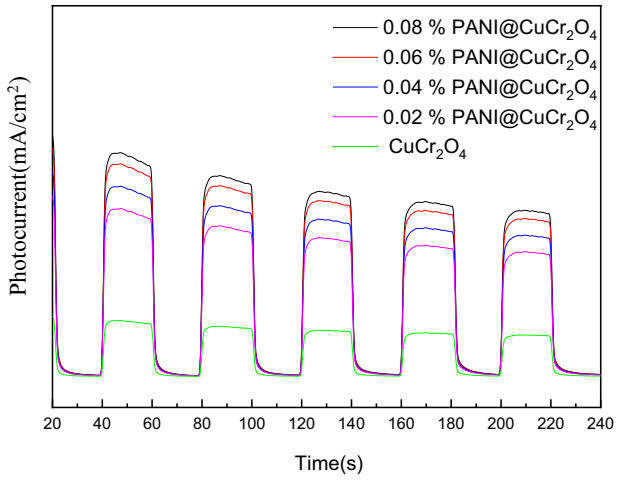

Fig. 8 Transient photocurrent responses of $CuCr_2O_4$ and PANI@$CuCr_2O_4$ samples

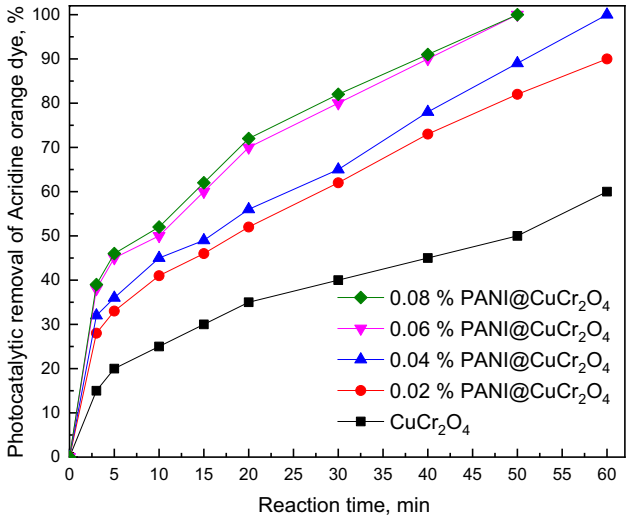

Fig. 9 Photocatalytic activities of $CuCr_2O_4$ and PANI@$CuCr_2O_4$ samples for degradation of acridine orange dye

contrary, the photocurrent transient responses for the diversity PANI@$CuCr_2O_4$ specimens are large when correlated to those of pure $CuCr_2O_4$ specimens. Furthermore, the transient photocurrent responses corresponding to the diverse fabricated nanocomposites are arranged in the following regulation; $CuCr_2O_4$ < 0.02% PANI@$CuCr_2O_4$ < 0.04% PANI@$CuCr_2O_4$ < 0.06% PANI@$CuCr_2O_4$ < 0.08% PANI@$CuCr_2O_4$. Hence, it could be terminated that 0.06% PANI@$CuCr_2O_4$ specimen possesses the greatest photocurrent response and in a similar way, the greatest photocatalytic efficacy.

Photocatalytic achievement investigation

Destruction of acridine orange (AO) dye has been inspected on the diversity fabricated PANI@$CuCr_2O_4$ nanocomposites so to assess their photocatalytic achievement (Fig. 9). The photocatalytic destruction of acridine orange dye was implemented beneath Vis light irradiation. Figure 9 elucidates that when the photocatalytic destruction of acridine orange dye is conducted over $CuCr_2O_4$ specimen, the destruction speed of the dye is found to be about 60% after 1 h under the consequence of Vis light irradiation. Whereas, the inclusion of 0.02%PANI to $CuCr_2O_4$ in the fabrication of 0.02% PANI@$CuCr_2O_4$ nanocomposite leads to an enhancement in the photocatalytic destruction speed of the dye to 90% after 1 h. Additionally, when the novel nanocomposites (0.04% PANI@$CuCr_2O_4$, 0.06% PANI@$CuCr_2O_4$, and 0.08% PANI@$CuCr_2O_4$) have been endorsed, the destruction speeds of acridine orange dye have been promoted up to 100% after diverse reaction times (60, 50 and 50 min, respectively) beneath Vis light irradiation. The attained data elucidate that 0.06% PANI@$CuCr_2O_4$ nanocomposite possesses the greatest photocatalytic efficiencies as compared to those of other fabricated specimens ($CuCr_2O_4$, 0.02% PANI@$CuCr_2O_4$, 0.04% PANI@$CuCr_2O_4$, and 0.08% PANI@$CuCr_2O_4$ specimens even if short exposure time is applied (50 min).

Figure 10 elucidates the consequence of photo-catalyst dose on acridine orange dye photocatalytic destruction. It is noticed from the data of Fig. 10 that enlarging nanocomposite (0.06% PANI@$CuCr_2O_4$) dose from 0.5 to 1.0 g/L brings about an enhancement in the photocatalytic activity of 0.06% PANI@$CuCr_2O_4$ photo-catalyst from 80 to 90% after 60 min. on the other hand, the time needed to complete the photocatalytic destruction of the dye is declined from 50 to 40 min if the catalyst does is boosted

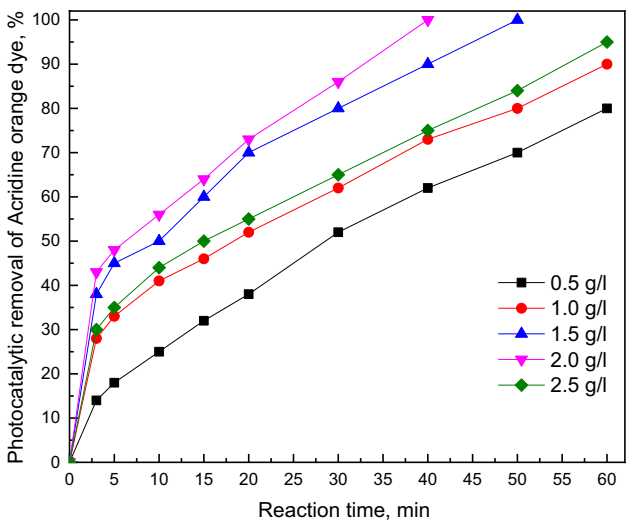

Fig. 10 Effect of dose of 0.06% PANI@ $CuCr_2O_4$ photocatalyst for degradation of acridine orange dye

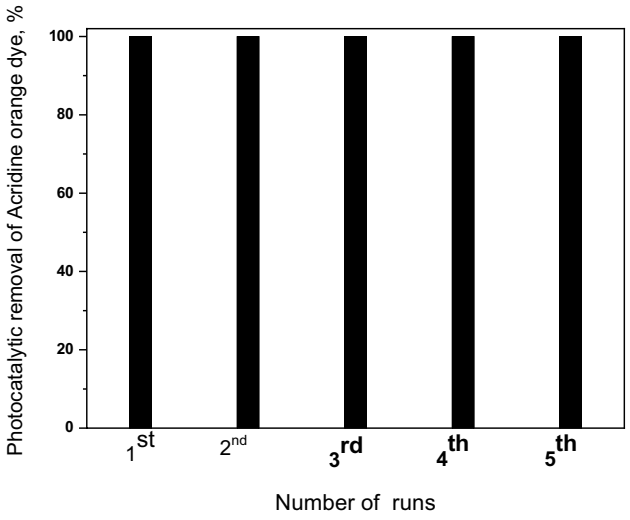

Fig. 11 Stability of 0.06% PANI@ $CuCr_2O_4$ photocatalyst towards the degradation of acridine orange dye after its application up to five times

from 1.5 to 2.0 g/L. It is obvious that enlarging of the catalyst dose (from 1.5 to 2.0 g/L) leads to a reduction in the time needed to complete the reaction (from 50 to 40 min) clarifying the enhancement in the photocatalytic efficiency, which might be associated with the upgrading of the feasible active centers. On contrary, utilization of higher dose of the fabricated photocatalyst (higher than 2.0 g/L) reduces the photocatalytic performance (down to 95%) at 1 h. This finding could be associated with the hindrance of Vis light dissipation to the surface of the photo-catalyst that retards acridine orange dye destruction.

Figure 11 exhibits the stability of 0.06% PANI@ $CuCr_2O_4$ nanocomposite towards the photocatalytic destruction of acridine orange dye upon its utilization up to five cycles. The observation of Fig. 11 affirms the greater stability of 0.06% PANI@$CuCr_2O_4$ nanocomposite upon its handling up to five times.

Conclusions

The outcomes of this investigation could be summarized as follows:

1. PANI@$CuCr_2O_4$ nanocomposite with the homogenous nanospherical design was successfully fabricated.
2. PANI@$CuCr_2O_4$ nanocomposite has been identified via FTIR, XPS, BET, XRD, TEM, and UV–Vis and PL analyses.
3. PANI@ $CuCr_2O_4$ nanocomposite could be utilized for acridine orange dye photocatalytic destruction beneath Vis light irradiation.
4. The photocatalytic performance of 0.06% PANI@ $CuCr_2O_4$ non-composite reached 100% towards the destruction of acridine orange dye after 40 min of Vis light exposure via utilization of 2.0 g/L of the photocatalyst.
5. 0.06% PANI@$CuCr_2O_4$ nanocomposite could be reutilized up to five times preserving its stability.

Acknowledgements This Project was funded by the Deanship of Scientific Research (DSR) at King Abdulaziz University, Jeddah, under grant no. G-98-130-40. The authors, therefore, acknowledge with thanks DSR for technical and financial support.

References

Acharyya SS, Ghosh S, Adak S, Tripathi D, Bal R (2015a) Fabrication of $CuCr_2O_4$ spinel nanoparticles: a potential catalyst for the selective oxidation of cycloalkanes via activation of Csp3–H bond. Catal Commun 59:145–150

Acharyya SS, Ghosh S, Siddiqui N, Sivakumar Konathala LN, Bal R (2015b) Cetyl alcohol mediated synthesis of $CuCr_2O_4$ spinel nanoparticles: a green catalyst for selective oxidation of aromatic C–H bonds with hydrogen peroxide. RSC Adv 5:4838–4843

Acharyya SS, Ghosh S, Tiwari R, Pendem C, Sasaki T, Bal R (2015c) Synergistic effect between ultrasmall Cu(II) oxide and $CuCr_2O_4$ spinel nanoparticles in selective hydroxylation of benzene to phenol with air as oxidant. ACS Catal 5:2850–2858

Aljahdali MS, Amin MS, Mohamed RM (2018) Gd-cobalt selenite as an efficient nanocomposite for aniline synthesis from the photocatalytic reduction of nitrobenzene. Mater Res Bull 99:161–167

An C, Wang S, Sun Y, Zhang Q, Zhang J, Wang C, Fang J (2016) Plasmonic silver incorporated silver halides for efficient photocatalysis. J Mater Chem A 4:4336–4352

Arboleda J, Echavarria A, Amparo Palacio L (2014) Synthesis and characterization of $(NH_4)_{1.5}Cu_2Cr_2O_8(OH)_{1.5}{\cdot}H_2O$. Powder Diffr 24:244–246

Baoum AA, Amin MS, Mohamed RM (2018) Decoration of SnO_2 nanosheets by AgI nanoparticles driven visible light for norfloxacin degradation. Appl Nanosci 8:2093–2102

Chen S, Cao G (2005) Study on the photocatalytic reduction of dichromate and photocatalytic oxidation of dichlorvos. Chemosphere 60:1308–1315

Delmon B (2007) Preparation of heterogeneous catalysts. J Therm Anal Calorim 90:49–65

Faisal M, Tariq AM, Muneer M (2007) Photocatalysed degradation of two selected dyes in UV-irradiated aqueous suspensions of titania. Dyes Pigments 72:233–239

Faisal M, Harraz FA, Ismail AA, Alsaiari MA, Al-Sayari SA, Al-Assiri MS (2019) Novel synthesis of polyaniline/$SrSnO_3$ nanocomposites with enhanced photocatalytic activity. Ceram Int 45:20484–20492

George K, Sugunan S (2008) Nickel substituted copper chromite spinels: preparation, characterization and catalytic activity in the oxidation reaction of ethylbenzene. Catal Commun 9:2149–2153

Girish S, Kumar KSR, Rao K (2017) Comparison of modification strategies towards enhanced charge carrier separation and photocatalytic degradation activity of metal oxide semiconductors (TiO_2, WO_3, and ZnO). Appl Surf Sci 391:124–148

Haghighat Mamaghani A, Haghighat F, Lee CS (2017) Photocatalytic oxidation technology for indoor environment air purification: the state-of-the-art. Appl Catal B Environ 203:247–269

Lee KM, Lai CW, Ngai KS, Juan JC (2016) Recent developments of zinc oxide based photocatalyst in water treatment technology: a review. Water Res 88:428–448

Liu L, Ding L, Liu Y, An W, Lin S, Liang Y, Cui W (2017) A stable Ag_3PO_4@PANI core@shell hybrid: enrichment photocatalytic degradation with p–p conjugation. Appl Catal B Environ 201:92–104

Radoicic M, Ciric-Marjanovic G, Spasojevic V, Ahrenkiel P, Mitric M, Novakovic T, Šaponjic Z (2017) Superior photocatalytic properties of carbonized PANI/TiO2 nanocomposites. Appl Catal B Environ 213:155–166

Ma P, Geng Q, Gao X, Yang S, Liu G (2016) $CuCr_2O_4$ spinel ceramic pigments synthesized by sol–gel self-combustion method for solar absorber coatings. J Mater Eng Perform 25:2814–2823

Mageshwari K, Sathyamoorthy R, Yong Lee J, Park J (2015) Novel $CuCr_2O_4$ embedded CuO nanocomposites for efficient photodegradation of organic dyes. Appl Surf Sci 353:95–102

Meng X, Zhang Z (2016) Bismuth-based photocatalytic semiconductors: introduction, challenges and possible approaches. J Mol Catal A Chem 423:533–549

Paul B, Bhuyan B, Purkayastha DD, Dhar SS, Behera S (2015) Facile synthesis of spinel $CuCr_2O_4$ nanoparticles and studies of their photocatalytic activity in degradation of some selected organic dyes. J Alloys Compd 648:629–635

Peng RY, Fan JH (2005) Ozonalytic kinetic order of dye decoloration in aqueous solution. Dyes Pigments 67:153–159

Rani M, Shanker U, Jassal V (2017) Recent strategies for removal and degradation of persistent and toxic organochlorine pesticides using nanoparticles: a review. J Environ Manag 190:208–222

Reddy PA, Reddy PVL, Kwon E, Kim KH, Akter T, Kalagara S (2016) Recent advances in the photocatalytic treatment of pollutants in aqueous media. Environ Int 91:94–103

Sanoop AP, Rajeev R, George BK (2015) Synthesis and characterization of a novel copper chromite catalyst for the thermal decomposition of ammonium perchlorate. Thermochim Acta 606:34–40

Shang M, Wang W, Sun S, Ren J, Zhou L, Zhang L (2009) Efficient visible light induced photocatalytic degradation of contaminant by spindle-like PANI/$BiVO_4$. J Phys Chem C 113:20228–20233

Sobahi TR, Amin MS (2019a) Synthesis of ZnO/ZnFe2O4/Pt nanoparticles heterojunction photocatalysts with superior photocatalytic activity. Ceram Int. https://doi.org/10.1016/j.ceramint.2019.10.073

Sobahi TR, Amin MS (2019b) Upgrading the photocatalytic achievement of g-C3N4 nanosheets along with decoration with Ag@TiO_2 nanospheres for the preparation of vitamin B3. Appl Nanosci. https://doi.org/10.1007/s13204-019-00960-3

Sobahi TR, Amin MS, Mohamed RM (2018) Enlargement of photocatalytic efficiency of $BaSnO_3$ by indium doping for thiophene degradation. Appl Nanosci 8:365–557

Sohabi T, Amin MS, Mohamed RM (2017) Photocatalytic degradation of methylene blue dye by F doped Co_3O_4 nanowires. Desalin Water Treat 74:346–353

Szczepanik B (2017) Photocatalytic degradation of organic contaminants over clay–TiO_2 nanocomposites: a review. Appl Clay Sci 141:227–239

Tanwar R, Kaur B, Kumar Mandal U (2017) Highly efficient and visible light driven $Ni_{0.5}Zn_{0.5}Fe_2O_4$@PANI modified BiOCl heterocomposite catalyst for water remediation. Appl Catal B Environ 211:305–322

Wang Q, Hui J, Li J, Cai Y, Yin S, Wang F, Su B (2013) Photodegradation of methyl orange with PANI-modified BiOCl photocatalyst under visible light irradiation. Appl Surf Sci 283:577–583

Wang S, Yun JH, Luo B, Butburee T, Peerakiatkhajohn P, Thaweesak S, Xiao M, Wang L (2017) Recent progress on visible light-responsive heterojunctions for photocatalytic applications. J Mater Sci Technol 33:1–22

Xie Y, Chen F, He J, Zhao J, Wang H (2000) Photoassisted degradation of dyes in the presence of Fe_3 and H_2O_2 under visible irradiation. J Photochem Photobiol A Chem 136:235–240

Yan J, Zhang L, Yang H, Tang Y, Lu Z, Guo S, Dai Y, Han Y, Yao M (2009) $CuCr_2O_4/TiO_2$ heterojunction for photocatalytic H_2 evolution under simulated sunlight irradiation. Sol Energy 83:1534–1539

Yuan W, Liu X, Li L (2014) Synthesis, characterization and photocatalytic activity of cubic-like $CuCr_2O_4$ for dye degradation under visible light irradiation. Appl Surf Sci 319:350–357

Zhang H, Zhu Y (2010) Significant visible photoactivity and antiphotocorrosion performance of CdS photocatalysts after monolayer polyaniline hybridization. J Phys Chem C 114:5822–5826

Zhang H, Zong R, Zhu Y (2009) Photocorrosion inhibition and photoactivity enhancement for zinc oxide via hybridization with monolayer polyaniline. J Phys Chem C 113:4605–4611

Zhao J, Ji M, Di J, Ge Y, Zhang P, Xia J, Li H (2017) Synthesis of g-$C_3N_4/Bi_4O_5Br_2$ via reactable ionic liquid and its cooperation effect for the enhanced photocatalytic behavior towards ciprofloxacin degradation. J Photochem Photobio A Chem 347:168–176